

Tailored Optical Functionality by Combining Electron-Beam and Focused Gold-Ion Beam Lithography for Solid and Inverse Coupled Plasmonic Nanostructures

Mario Hentschel,* Julian Karst, and Harald Giessen*

Plasmonics is a field uniquely driven by advances in micro- and nanofabrication. Many design ideas pose significant challenges in their experimental realization and test the limits of modern fabrication techniques. Here, the combination of electron-beam and gold ion-beam lithography is introduced as an alternative and highly versatile route for the fabrication of complex and high fidelity plasmonic nanostructures. The capability of this strategy is demonstrated on a selection of planar as well as 3D nanostructures. Large area and extremely accurate structures are presented with little to no defects and errors. These structures exhibit exceptional quality in shape fidelity and alignment precision. The combination of the two techniques makes full use of their complementary capabilities for the realization of complex plasmonic structures with superior optical properties and functionalities as well as ultra-distinct spectral features which will find wide application in plasmonics, nanooptics, metasurfaces, plasmonic sensing, and similar areas.


1. Introduction

The field of plasmonics has mainly been driven by innovation in fabrication techniques. Early on, many theoretical investigations predicated unprecedented, peculiar, and fascinating optical properties.^[1–4] However, simulations and experiments showed sizable differences not only in the realized geometries, but also and in particular in the optical properties. Many theoretical designs in fact posed significant challenges when realizing them experimentally. The reasons are multifold and include small sizes, complexity, structural composition, 3D arrangements, shape accuracy, or material composition. Bottom-up techniques, such as wet chemical nanoparticles synthesis, have been among the first techniques used.^[5–7] However,

while these techniques can produce large amounts of plasmonic structures, they struggle as soon as complex arrangements of different nanoparticles are needed, possibly even distributed on large areas as well as in periodic arrangements. Only recently, with the advent of sophisticated DNA-guided nanotechnology, also in combination with other techniques, it became possible to create such structures.^[8–11] In contrast, top-down techniques such as optical lithography and electron-beam lithography straightforwardly offer the required periodic and well defined arrangement on surfaces. Taking these techniques a step further, they are also able to realize 3D arrangements by virtue of mark recognition and layered fabrication.^[12] Additionally, these top down techniques allow for a larger variety of

structures and can be used to fabricate solid particles of almost any metal or dielectric as well as inverse structures, such as slits and holes in metallic and dielectric films employing Babinet's principle.^[13] Electron-beam lithography (EBL) has been utilized for many years and is a prime candidate for highest resolution structuring and layered processes. Using positive and negative tone resists, lift-off, reactive and non-reactive ion (beam) etching, a plethora of solid and inverse structures can be fabricated.^[14,15] The technique, however, faces a few limitations: The fabrication of "sculptured" structures, that is, of structures with varying thickness or shape or of particles with complex 3D shapes, is extremely difficult if not impossible. While EBL gray-scale lithography can be applied in some cases, this technique is intrinsically process-unstable and difficult to control. Another limitation lies with the EBL resists as not all samples or structures tolerate resists, either due to contamination issues, due to the fragility of the substrate, for example, in case of transmission electron microscopy (TEM) membranes, or due to very small sample sizes which do not allow for homogeneous resist spin coating. In some of these cases the use of a focused ion-beam (FIB) tool has proven successful.^[16,17] Here, a beam of focused ions sputters and allows to structure the material of interest directly.^[18–21] The main use of these so-called cross beam tools, consisting of a (crossed) scanning electron column and a focused ion beam column, lies with the fabrication of TEM cuts and lamellas for material inspection. Consequently, the resolution of these tools is limited in two aspects: For so-called FIB cuts as well as TEM lamella production large amounts of material have to be removed which

Dr. M. Hentschel, J. Karst, Prof. H. Giessen
4th Physics Institute and Research Center SCoPE
University of Stuttgart
Pfaffenwaldring 57, Stuttgart 70569, Germany
E-mail: m.hentschel@physik.uni-stuttgart.de; giessen@pi4.uni-stuttgart.de

 The ORCID identification number(s) for the author(s) of this article can be found under <https://doi.org/10.1002/adom.202000879>.

© 2020 The Authors. Published by WILEY-VCH Verlag GmbH & Co. KGaA, Weinheim. This is an open access article under the terms of the Creative Commons Attribution License, which permits use, distribution and reproduction in any medium, provided the original work is properly cited.

Kindly note that open access information regarding "Project DEAL" have been added on 15 October 2020 after initial publication.

DOI: 10.1002/adom.202000879

calls for large beam currents and thus limits the resolution. Moreover, the sample is mounted on standard sample stages with micrometer positioning accuracy which does not allow for high precision overlay processes as needed for complex plasmonic structures. Another important issue lies with the ions used in such tools: Standard FIB tools use a liquid metal source in which a tungsten tip is covered with a film of liquid metal from which the ions are drawn. Due to its low melting point, gallium (Ga) has become the workhorse. Structuring materials with a beam of focused Ga ions will unavoidably lead to the incorporation of ions in the material of interest as the Ga ions cannot diffuse out of the material. This is in stark contrast to techniques such as argon ion beam etching where argon ions are being used. Significant efforts have been undertaken to investigate the degree of incorporation in the structured materials and it was shown that a clear-cut answer is very difficult.^[16] It should be noted, that in all cases in which the material of interest is a thin film or a thin sheet, one can structure all the way through the material and move the region of ion implantation to the substrate material, strongly mitigating the influence.

In this article, we introduce a top-down fabrication scheme that makes use of another technological advance and utilizes the combination of EBL and true gold ion-beam lithography (IBL). While EBL has taken significant advantages due to the excellent focusability and thus highest resolution as well as laser interferometric sample stages for overlay processes, typical ion-beam tools suffered from comparably poor focusability and the lack of a laser interferometric sample stage. These drawbacks also hindered mix and match processes between the two techniques which would make use of their complementary structuring capabilities. We use the combination of the dedicated lithography tools eLine Plus and ionLine Plus (now replaced by the Velion) from Raith GmbH to overcome these issues. The ionLine Plus utilizes a eutectic of gold and silicon with a melting point around 300 °C as ion source, thus allowing to structure with silicon (Si) as well as gold (Au) ions by virtue of an additional Wien filter. The tool offers optimized beam parameters, such as diminishing the beam tails known from standard ion-beam tools, at the cost of a reduced beam current. The also implemented laser interferometric sample stage now allows standard mark-based overlay processes well known from EBL. The use of Au ions enables contamination free structuring of gold structures,^[22,23] which are still the prime choice in plasmonics.

Combining these two techniques, we present large area and extremely accurate structures with little to no defects and errors, demonstrating exceptional quality in shape fidelity and alignment precision. This allows us to make full use of their complementary capabilities for combined complex plasmonic structures with superior optical properties and functionalities as well as ultra-distinct spectral features. In the following, we present a collection of well-studied as well as entirely novel complex plasmonic structures to demonstrate the strength of this combined fabrication strategy.

2. Results and Discussion

Figure 1 illustrates the main idea behind the combination of EBL and IBL and the mutual benefits of the complementary

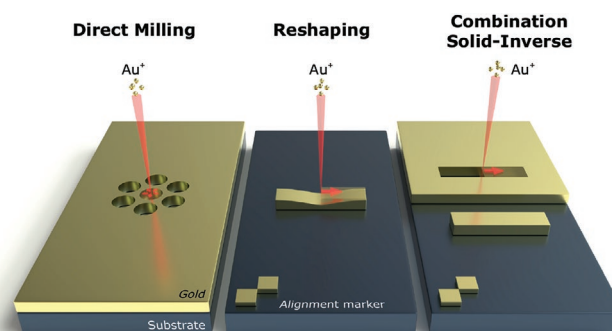


Figure 1. The combination of electron-beam and ion-beam lithography allows for novel fabrication schemes of complex plasmonic nanostructures. Each technique is used for the task best-suited to the respective properties. Inverse structures can be milled with Au⁺ ions without any contamination issues into Au films. Solid structures are best fabricated via EBL. Both processes can be combined and overlaid with the help of mark recognition to fabricate inverse and solid structures side by side, on-top of each other, or to re-shape solid structures by selective removal of material.

properties of the two techniques for advanced nanostructuring in plasmonics. Inverse plasmonic structures, such as the plasmonic oligomer shown on the left, can be most straightforwardly fabricated by direct milling. The focused Au⁺ ion-beam directly mills the bulk Au material without the need for any resists and without any potential contamination of the Au film itself. The middle icon illustrates the reshaping and manipulation of an Au nanostructure. This structure could, for example, be defined by EBL and then reshaped and sculpted with the Au⁺ ion-beam. As the deposited dose of the ion-beam determines the milling depth, IBL is an intrinsic gray-scale lithographic process and thus allows to shape forms in three dimensions.^[24] In this particular example, the beam trims and thins the center of a gold nanorod, which would not be possible with EBL alone. The precise alignment of the two subsequent EBL and IBL process steps is accomplished by mark recognition, as indicated by the alignment maker sketched in the icon. The third example on the right depicts the combination of inverse and solid plasmonic structures. Again, each part of the structure is fabricated by the technique best-suited to accomplish the goal: An EBL based lift-off process for the solid rod and direct Au⁺ ion-beam milling for the inverse structure. The alignment is again ensured by mark recognition.

Figure 2 depicts scanning electron microscopy (SEM) images illustrating a number of examples. The top row shows solid nanorods as well as nanodiscs which have been fabricated via standard EBL based lift-off. Afterward, IBL is used to reshape the nanostructures. In case of the rods, different numbers of indentations have been created to make them work as gap antennas. Such a structure cannot be obtained by simple EBL as the topography and thickness of the metallic film will always be of homogeneous thickness. In case of the discs, IBL was used to remove part of the discs and change the dimensions. In particular, the disc with the cut-out center part and the remaining thin outer rim, which is on the order of 15 nm, illustrates the high resolution of IBL. The circular arrangements of nanoholes of ≈100 nm diameter has been milled into a 50 nm thick Au film on a 50 nm thick silicon nitride TEM membrane.^[25] This example underpins, first, the benefit of direct structuring

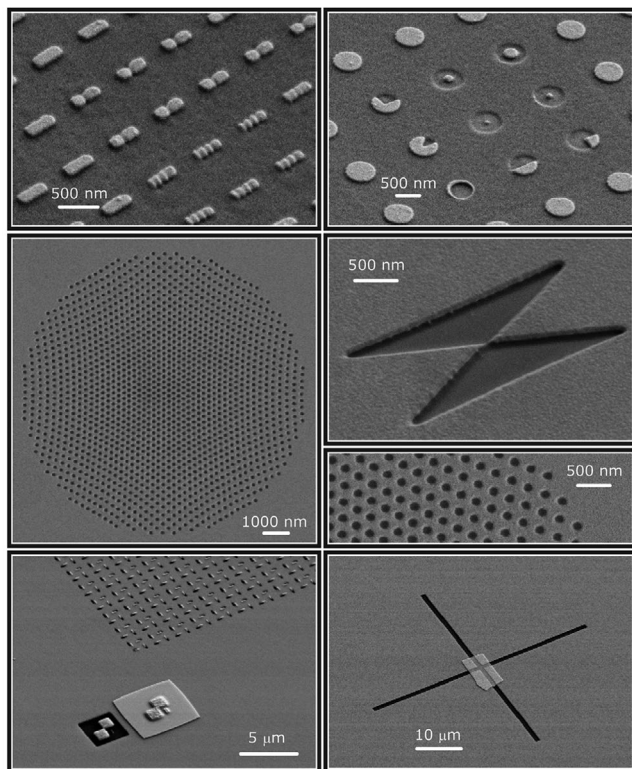


Figure 2. Scanning electron microscopy images of solid and inverse metallic nanostructures fabricated by EBL, IBL, and combination of both (top left to bottom right): EBL fabricated Au nanorods and nanodisks have been trimmed by IBL; an Au thin film on-top a silicon nitride TEM membrane has been structured by IBL (overview and close-up), an inverse bowtie antenna in an Au film fabricated by IBL, standard interwritefield alignment marks fabricated in an Au film by IBL together with the inverse plasmonic nanostructures and used to align the second layer EBL step, a larger inverse cross in an Au film made by IBL and used for coarse alignment of the EBL step.

without the need of resists, which are challenging to spin-coat on TEM membranes, and second, the excellent resolution as seen in the close-up of the structure. IBL can also be used to fabricate inverse bowtie antennas with gaps as small as 15 nm. The lower row shows different alignment marks used throughout this work. We use inter writefield alignment marks for highest accuracy alignment, as shown on the left. In this example, 150 nm thick copper marks haven been fabricated by EBL on the 50 nm thick Au film and are used to align the first layer IBL step (the mark on the left, processing caused the milled-away Au film and thinned copper mark) and the second layer EBL step (mark on the right, processing caused the additional Au film on-top). The image on the right illustrates a larger inverse cross mark milled by IBL and used for a coarser alignment in a second layer EBL step.

The fabrication parameters used in EBL and IBL are mainly unchanged throughout this manuscript and are as follows: For EBL we use a double layer PMMA resist exposed using the Raith eLine Plus system at 20 kV acceleration voltage. For IBL we utilize the Raith ionLine Plus system (now replaced by the Raith Velion) equipped with the multispecies column, allowing for the use of singly or doubly charged silicon (Si) or

gold (Au) ions at fixed 35 kV acceleration voltage. In order to prevent any contamination of our gold nanostructures, we use Au⁺ ions with a beam limiting aperture of 10 μm. Area dose values vary significantly depending on the milling depth, the structure width, etc. and require careful calibration as IBL is in general less stable compared to EBL. All optical spectra shown throughout the manuscript are measured with a Fourier Transform Infrared spectrometer (Bruker Vertex 80), equipped with a microscope (Hyperion 3000) and a mercury cadmium telluride detector. More details can be found in the experimental section.

One system that attracted considerable interest in the plasmonics community is the so-called plasmonic analogue of electromagnetically induced transparency (EIT).^[12,26–28] In the most common realization of this system, a bright dipolar plasmonic mode supported by a single nanorod is near-field coupled to a plasmonic mode comprised of an out-of-phase oscillation of two dipolar modes in a pair of parallel nanorods as coupled classical oscillators.^[29] In the symmetric system, in which the single rod lies centered between the rod pair, an external light field polarized along the long axis of the single rod will excite the bright dipolar mode which results in a dip in transmission. Inducing asymmetry will cause energy transfer between the bright and dark modes and reshaping of the spectral signatures. As a consequence, a transmission window of enhanced transmission opens within the former transmission minimum.

Applying the so-called Babinet principle,^[13,30] one can transform this structure into an inverse one in which a single nanoslit and a pair of parallel nanoslits cause the bright and dark modes. Due to Babinet's principle, the roles of reflection and transmission as well as the polarization directions are reversed. **Figure 3** depicts the measured spectra as well as SEM images of this a so-called planar plasmonic analogue of electromagnetically induced transparency (EIT).^[17] In the bottom image, we show an overview of the structure with the strongest displacement. All arrays have a size of 100 × 100 μm² and have been milled with IBL into a 40 nm thick Au film on a glass substrate (Suprasil, Heraeus). The main challenges with the fabrication are related to good shape fidelity as well as a small ridge width between adjacent slits for efficient coupling, minimizing parasitic milling of these ridges. The image underlines the excellent structure quality obtained with IBL, measuring a remaining ridge width on the order of 20 nm. We now turn our attention to the optical response. For the structure outlined in blue the single slit is centered between the pair of slits. Thus, no near-field coupling is possible and we observe a single dip in reflectance, as expected. With increasing displacement, a peak of reflectance opens, reaching sizable modulation for the maximum displacement (red and black, respectively). This sharp spectral feature is only possible when most of the individual EIT structures exhibit the same shape fidelity, and disorder due to fabrication errors can be neglected. Therefore, the spectral functionality is proof of the superior quality of the IBL system in use.

Coupling phenomena between individual plasmonic elements are a central aspect of complex plasmonics.^[1] So-called plasmonic oligomers composed of densely packed hexagonal arrangements of individual disks are a particularly interesting example.^[31,32] The individual discs each support two energetically degenerate in-plane dipolar modes. If the interparticle

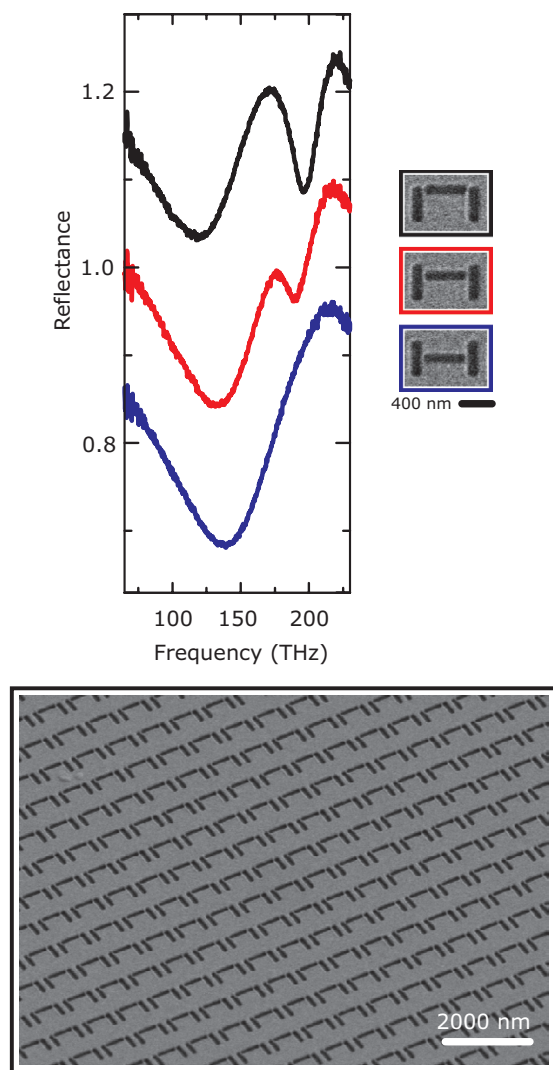


Figure 3. Measured spectra as well as SEM images of the planar plasmonic analogue of electromagnetically induced transparency (EIT). Top half: Increasing the asymmetry in the structure by displacing the single horizontal nanoslit results in an increased coupling to a dark mode comprised of an out-of-phase oscillation of the two dipolar modes supported by the pair of parallel slits. Thus, a window of enhanced reflectance opens within the reflectance dip of the fully symmetric structure. Bottom half: Overview SEM image of the structure with strongest coupling, underpinning the excellent large area fabrication quality. The length \times width of the dipole slit is $400 \text{ nm} \times 70 \text{ nm}$, quadrupole wires $360 \text{ nm} \times 70 \text{ nm}$, ridge width $\approx 20 \text{ nm}$, periodicity is 800 nm in both directions, film thickness 40 nm Au . The spectra are shifted upward by 0.2 for clarity.

distance is small enough, the modes couple and give rise to new truly collective modes, similarly to the formation of molecular orbitals.^[33] These modes possess different properties in comparison to the original dipolar modes of the individual particles. Most prominently, many of them are in fact dark modes with significantly longer life times and thus larger field enhancement. Equivalent to the plasmonic analogue of EIT, also in these structures the interaction of bright and dark modes leads to the formation of a Fano resonance^[34–37] and an accompanying transmission window as a spectral sign of this

phenomenon.^[38–40] Due to the significant field enhancement, these structures are particularly sensitive to changes in their immediate surroundings and found application in many plasmonic sensing schemes.^[40,41] It is thus important to enhance the interaction of the modes with their environment as much as possible. One way to accomplish this lies with the creation of inverse oligomer structures, as shown in **Figure 4**.^[42] Here, the seven discs become circular holes in a continuous metallic film which are ideal in a plasmonic sensing application. IBL is the ideal method to fabricate such structures. The key challenge in the fabrication is the realization of as small ridges between the individual holes to ensure the strongest coupling. Moreover, applications often require larger arrays of identical structures, demanding highest precision and stability of the milling process.

The SEM image in **Figure 4** demonstrates the excellent fabrication quality and homogeneity over the entire $100 \times 100 \mu\text{m}^2$ array. Also, the periodicity is well preserved and no drift can be observed, an artifact which often occurs with standard FIB sample stages. In order to study the transition from isolated to collective modes and the increase in interaction strength, we fabricated four arrays with varying interparticle distance. For the largest separation (green) of 130 nm , we observe first coupling phenomena, yet the overall spectrum still partially resembles the spectrum of isolated discs. Reducing the gap size to 100 nm , we observe a sizable broadening of the entire spectral feature consistent with the formation of a coupled super-radiant mode as well as the emergence of a Fano resonance around 1500 nm , indicating the presence of the dark mode. Both trends continue for a further reduction of the interparticle distance down to 80 and 60 nm . For the smallest separation and ridge width we observe a spectrally extremely broad super-radiant mode profile as well as a well-modulated Fano resonance. This can only be observed if the sample is extremely homogeneous over its entire area.

Often theoretical predictions or application requirements call for 3D structures. Layered, mark-based fabrication based on EBL and IBL can straightforwardly offer such functionalities. In such cases, the required nanostructures are divided into individual layers which are subsequently fabricated. The alignment and tuning of coupling strength is ensured by mark-recognition and vertical spacer layers based on spin-coatable polymers. To demonstrate the strength of combining EBL and IBL, we proceed with the fabrication of the previously studied solid inverse plasmonic EIT structure,^[43] depicted in **Figure 5**. It has been shown that the coupling between solid and inverse plasmonic structures is possible when considering certain design rules. In the current system, the dark mode is formed in a pair of parallel slits in a 40 nm thick gold film in the first layer, as sketched in panel a). The dipolar resonances associated with each slit can be viewed as magnetic dipoles (green arrows), giving rise to a dark mode with out-of-phase oscillation of these two magnetic dipoles. Consequently, the largest electric near-field strength is expected in the center of the rod pair as well as above and below (indicated by the plus and minus signs). Coupling of the dipolar plasmonic mode of the solid rod, which is fabricated by EBL in the second layer, to this mode is thus possible by positioning the rod in the center and aligning the axes (which is due to the interchange of polarization directions

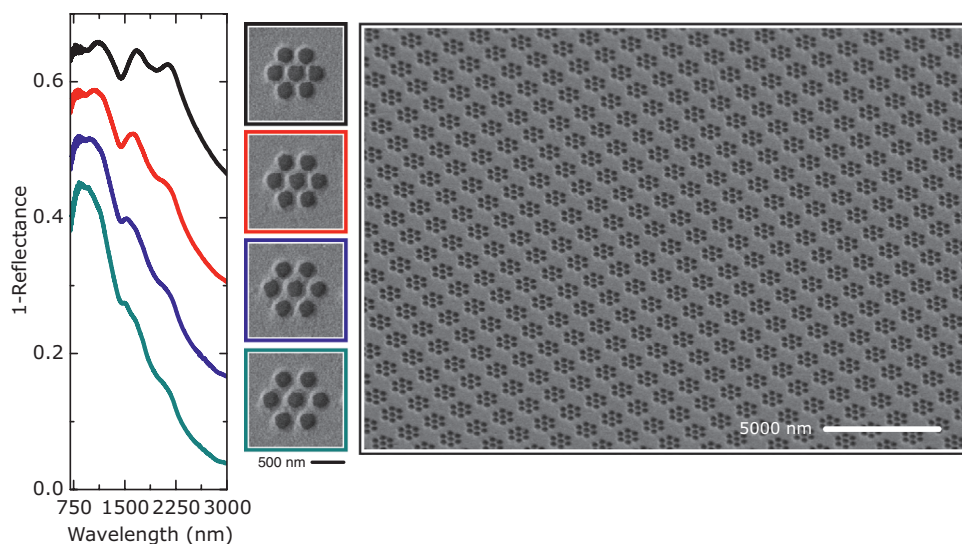


Figure 4. Measured spectra as well as SEM images of inverse plasmonic oligomers fabricated by IBL. Reducing the interparticle distance or ridge width of the individual particles leads to the emergence of a spectrally very broad mode profile indicating the formation of a super-radiant plasmonic mode spanning all seven nanoholes. Simultaneously, we observe the onset and the further development of a Fano resonance around 1500 nm which confirms the interaction of the bright super-radiant mode with a dark collective plasmon mode. The holes have a diameter of 230 nm, the interparticle distances are 130, 100, 80, 60 nm, respectively, periodicity 1500 nm in both directions. The spectra are shifted upward by 0.1 for clarity.

due to Babinet's principle), see sketch. One can see that in this geometry the areas of large electric field strength overlap, which indicates significant modal overlap. A 30 nm thick spin-coated polymer layer (PC403, JCR) serves as spacer layer and

ensures sufficient near-field coupling between the solid and inverse structures.

Figure 5 depicts the SEM images as well as the optical response of the solid inverse plasmonic EIT. For the

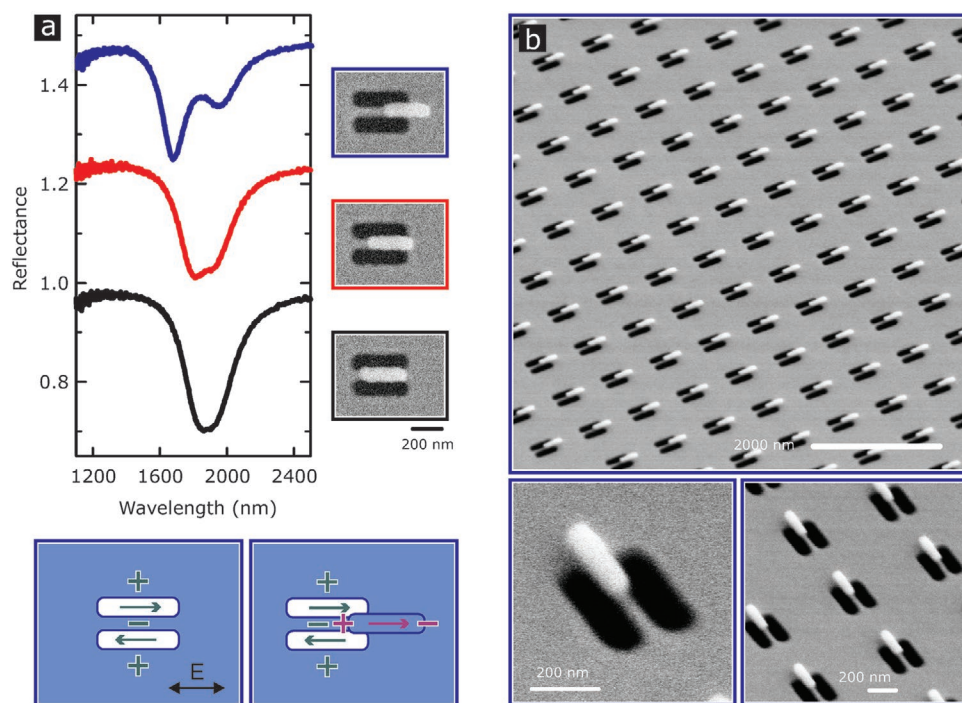


Figure 5. Solid-inverse plasmonic analog of EIT. a) Reflectance spectra of the structure for increasing symmetry breaking. One observes the widening of the resonance signature as well as the formation of a reflectance peak. The lower half illustrates the coupling between the inverse and solid structures in terms of the electric near-field distributions associated with the induced magnetic (green) and electric (purple) dipole moments. b) Tilted view SEM images of the structures, underpinning the excellent alignment accuracy and homogeneity of the structures. The length \times width of the quadrupole slits is 340 nm \times 100 nm, of the solid dipole 270 nm \times 85 nm, Periodicity is 800 nm in both directions, film thicknesses are 40 nm. The spectra are shifted upward by 0.2 for clarity.

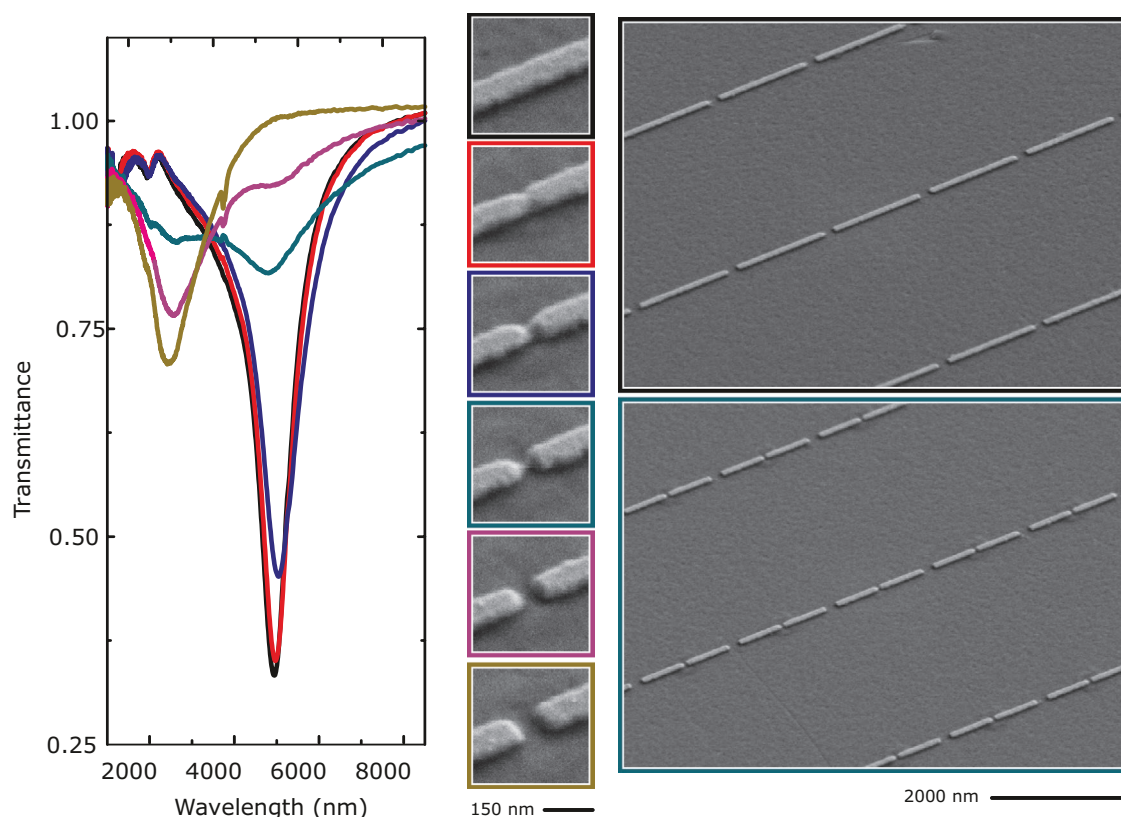


Figure 6. Combined and overlaid EBL and IBL for antenna modification and gap shaping. EBL fabricated Au antennas are modified by an ion beam to successively sputter away the center region and create gap antennas. The corresponding spectra clearly show a significant spectral reorganization that is caused by the effective antenna thinning, the creation of a gap, and the presence of charge-transfer as well as coupled dipolar modes. The SEM images display close-ups of the center region of the antennas, as well as two overview images. The antenna dimensions are $1350 \text{ nm} \times 100 \text{ nm}$, period $P_x = 1550$, $P_y = 3300 \text{ nm}$, thickness 40 nm .

symmetric structures, shown in black, no coupling to the dark mode is possible and one observes the spectral signature of a single dipolar resonance. Displacing the solid rod from its symmetric position (red), leads to the formation of a small resonant feature in the spectrum, indicating the opening of a reflection window. Simultaneously, we observe the widening of the entire spectral feature, underlining the onset of plasmonic coupling. For the largest displacement (blue) a clear reflection peak can be observed at the former reflection minimum. The tilted and normal view SEM images in Figure 5b demonstrate the excellent overlay accuracy and homogeneity of the fabricated structures, which is also the prerequisite to observe the sharp features in the optical spectrum (blue line) of Figure 5a.

One of the most prominent and unique features of IBL is its ability to re-shape structures as well as to perform gray-scale processes due to the direct link between the deposited dose and the milling depth. **Figure 6** depicts an example underpinning this special feature. Using EBL, infrared resonant nanoantenna arrays have been fabricated. Using mark recognition, IBL is used to successively cut the individual antennas in the array into gap antennas. The close-up SEM images in Figure 6 depict the center section of these antennas and illustrate the step-by-step cutting of the gap. The original antenna (black) exhibits a plasmonic resonance around $\sim 5000 \text{ nm}$. For the structure

shown in red we observe a clear narrowing of the center section of the antenna, material has been sputtered away on top as well as on the antenna sidewalls. It is important to stress that we benefit significantly from the use of Au^+ ions for the milling process as primary ions will be implanting into the antenna material which, in this case, will not lead to contamination. In the spectra we observe a slight decrease in resonance amplitude and a minute red-shift. Cutting deeper into the antenna center (blue), the resonance shifts further to the red and we observe a sizable reduction in the modulation depth. We attribute these effects to an effective “thinning” of the entire antenna which is generally expected to cause a spectral red-shift of the antenna. The reduction in modulation depth is also related to the effective reduction in antenna volume and thus a reduction in oscillator strength which is fundamentally linked to the number of quasi-free electrons. Further increasing the milling dose (green) leads to a pronounced change in the optical response. We observe two resonant signatures in the spectrum, one roughly at the position of the original antenna and one around $\sim 2200 \text{ nm}$. Inspecting the close-up SEM image, we see that the remaining ridge connecting the two antenna arms has now become extremely narrow. Thus, we effectively observe two different modes: A so-called charge transfer mode which still allows the excitation of a plasmonic mode spanning the entire structure close to the unperturbed system and

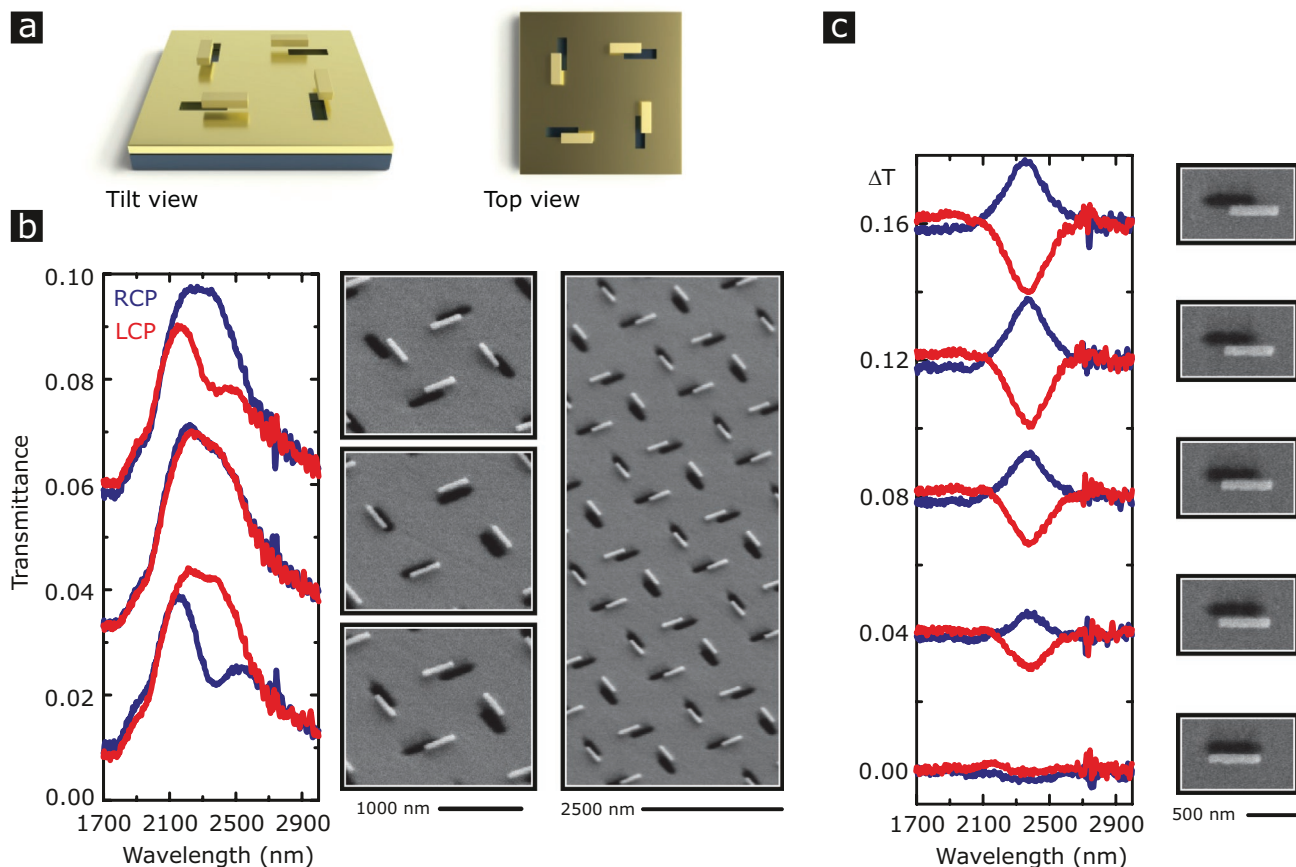


Figure 7. Mixed solid-inverse chiral plasmonic nanostructures. a) Sketches of the two-layered geometry consisting of slits in an Au film and solid Au rods in a C_4 symmetric arrangement. b) Transmittance spectra for RCP and LCP excitation for the two enantiomers and the achiral structure as well as tilted view SEM images. The spectra are shifted upward by 0.02 for clarity. c) Chiroptical response of the two enantiomers (blue and red, respectively) from increasing asymmetry (displacement of the slit and solid rod). The rod and slit dimensions are 400 nm \times 100 nm, super cell periodicity is 1000 nm in both directions, film thicknesses are 40 nm. The spectra are shifted upward by 0.04 for clarity.

additionally,^[44] due to the strong corrugation, we can excite the in-phase mode of dipolar excitations in each “half-antenna”. This mode is at significantly higher energy and is spectrally much closer to the mode of clearly split half-antennas when compared to the mode of the unperturbed entire antenna. It should be noted that most probably a few antennas are fully cut which will only support the in-phase coupled dipolar mode. Cutting even deeper (pink), the higher energy coupled mode gains in modulation, while the spectral signature of the unperturbed and charge transfer modes vanishes almost completely. A further increase of the ion dose results in a full cut through all antennas in the array, leaving only the spectral signature of the coupled in-phase mode of the dipolar resonances of the two half-antennas (light green). The overview SEM images portrait the original antennas in the upper panel and the fully cut ones in the lower panel. It is noteworthy that such a successive gap manipulation and reshaping of antenna fields on the same substrate is only possible by IBL as true gray-scale process which benefits from the direct link between the deposited dose and the milling depth.

As final example, we turn our attention to plasmonic chirality. This field has attracted significant interest over the last years, not only because of the fundamental importance

of chirality in nature but also because of the strong and tunable chiroptical response in plasmonic systems.^[45–52] Optical chirality, that is, the different response of a system to left and right circularly polarized light (LCP, RPC, respectively), is an intrinsically 3D property that requires advanced fabrication strategies.^[53–55] Also, it was shown that even minute changes to the morphology result in sizable changes in the chiroptical response,^[56] further underlining the fabrication challenges and the requirement of high accuracy planar and 3D nanofabrication. Top-down techniques have the benefit of straightforward structural modification and allow changing the asymmetry of the system, for example, to switch the response on and off.

Figure 7a depicts the design of our novel 3D chiral structure. We combine solid and inverse nanostructures, further outlining the additional degrees of design freedom afforded by our ansatz. The first layer is composed of individual nanoslits fabricated via IBL in a 40 nm thick Au film. Each slit supports a plasmonic resonance which can be viewed as a magnetic dipole moment. The second layer of solid plasmonic nanorods is fabricated by EBL and separated from the first layer by a spin-coated 30 nm thick polymer layer (PC403, JCR). The top view sketch in panel a indicates that the solid rods are displaced from the long axis of the nanoslit as well as from the center

position. The first displacement enables the rods to couple via near-field interaction to the nanoslits. The mutual interaction is best visualized in terms of electric near-fields. These are strongest in the central region of the nanoslit, that is, as a ring current around the magnetic dipole moment in the sample plane. The displacement along the mutual long axis is used to tune the degree of asymmetry in the structure and thus the strength of the chiroptical response. The positioning of the solid rod above or below the center axis determines the handedness of the system, resulting in the two enantiomers with tunable degree of asymmetry as well as the achiral species. The C_4 symmetric arrangement renders the system uniaxial and thus prevents polarization conversion in the system.

Figure 7b depicts the transmission spectra of the two enantiomers and the achiral structure for RCP and LCP excitation as well as close-up and tilted overview SEM images. The optical response for RCP and LCP excitation for the achiral structure is close to identical, as expected. We observe strong spectral mode signatures around ≈ 2200 nm which stem from the interaction of the two fundamental dipolar modes in the slit and the solid rod. For the two chiral structures, we observe a strongly different response: RCP and LCP excitation lead to significantly different mode signatures in the spectra. Again, we observe two distinct modes which we attribute to the bonding and anti-bonding combination of the two fundamental dipolar modes in the system. We can clearly see that the role of the handedness of the light and the structure interchange, as expected. Already in these spectra we see the strong chiroptical response of the plasmonic structures.

Figure 7c depicts the chiroptical response of the two enantiomers (blue and red, respectively) for increasing asymmetry (as indicated by the close-up SEM images). The achiral structure (bottom spectra and image) exhibits very little chiroptical signal, as expected from the spectra displayed in Figure 7b. With increasing displacement between the slit and the solid rod we observe the continuous increase of a mode signature at ≈ 2300 nm, which reaches its maximum for maximum displacement. The strength of the chiroptical signal is thus directly linked to the degree of structural asymmetry, as expected. The system in fact shows a remarkable ability to encode the 3D arrangement into the spectral response.

To further understand the nature of the resonant modes in the structure, one has to inspect the plasmonic near-field distributions. Figure 8 displays the simulated near-field distributions of the mixed solid-inverse structure under RCP excitation. The fields are shown at the spectral position of the signatures of the plasmonics modes, which in simulation occur around 2540 and 2140 nm, respectively, and depict the normal field components at each interface. In this mixed solid-inverse structure, it is necessary to inspect the electric and magnetic field distributions. The left column of Figure 8 depicts the z-component of the electric field, the right column the z-component of the magnetic field. In the electric field distributions, we can identify the dipolar pattern associated with the fundamental mode of the solid rod, which is characterized by an electric dipole moment. Likewise, we can identify magnetic dipole moments in the magnetic field distributions, which are associated with the fundamental mode of the slits. The lower energy mode at 2540 nm is characterized with the bonding out-of-phase combination of the electric and magnetic dipole moments, while the

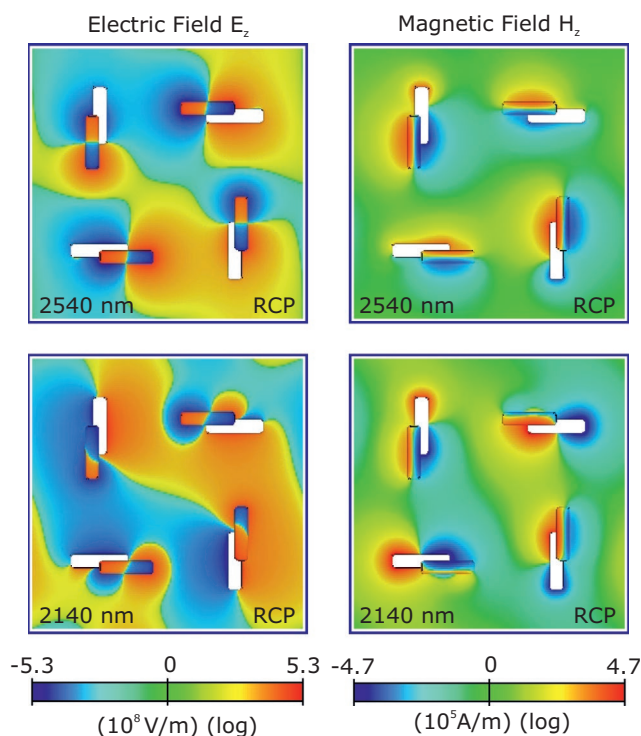


Figure 8. Simulated near-field distributions of the mixed solid-inverse chiral plasmonic nanostructures under RCP excitation. The left column depicts the z-component of the electric near field, the right column the z-component of the magnetic field at the spectral positions of the plasmonic resonant features. Inspecting the modes, one finds that the lower energy mode is characterized by an out-of-phase combination of the electric and magnetic moments associated with the solid rods and slits, while the higher energy mode consists of the in-phase and thus energetically less favorable combination.

higher energy mode at 2140 nm is characterized by an in-phase combination.

3. Conclusions

We have introduced a fabrication strategy combining electron-beam and gold ion-beam lithography for complex plasmonic nanostructuring. We have demonstrated that the straightforward mix-and-match processes between EBL and IBL allow for complex structures, benefiting from the complementary properties of the two techniques. We have fabricated single-layered structures milling Au films with Au^+ ions with excellent resolution, accuracy, and shape fidelity while additionally preventing any contamination of the material due to implantation of the primary ion-beam. IBL in combination with EBL has also proven highly intriguing for the re-shaping of plasmonic nanostructures, resulting in the ability to tune and manipulate the optical response. Utilizing spin-coatable dielectric polymer spacers, we have demonstrated 3D structures composed of solid and inverse nanostructures fabricated in subsequent EBL and IBL processes. We believe that this new ansatz significantly expands the fabrication tool kit and will find applications in plasmonics, nanooptics, plasmonic sensing, and similar areas.

4. Experimental Section

The fabrication parameters used in EBL and IBL are mainly unchanged throughout this manuscript and are as follows: For EBL, a double layer PMMA resist combination made of a 200 K \approx 200 nm thick first layer and a 950 K \approx 50 nm thick second layer (Allresist AR-P 642 and AR-P 672) was used. For nonconductive substrates, an additional conductive water-soluble polymer (Espacer, Showa Denko) was spin-coated as the last layer. All structures were exposed using the Raith eLine Plus system at 20 kV acceleration voltage and a beam limiting aperture of 20 μ m, resulting in a beam current of approximately 150 pA. Depending on the write field size (200 or 100 μ m), 5 or 6 nm step sizes were used, respectively, at an area dose of 325 μ C cm⁻². For IBL, the Raith ionLine Plus system (now replaced by the Raith Velion) equipped with the multispecies column, was utilized, allowing for the use of singly or doubly charged silicon (Si) or gold (Au) ions at fixed 35 kV acceleration voltage. In order to prevent any contamination of the gold nanostructures, Au⁺²⁺ ions were used. It was found that the resolution and milling rate for structuring Au with Au⁺²⁺ ions only weakly depend on the ionization state of the ion. The doubly charged ions have twice the energy, yet the beam current is lower compared to the singly charged species. Thus, singly charged ions and a beam limiting aperture of 10 μ m were used. The resulting beam current changed significantly over time as the aperture was milled open during structuring. A slight reduction in resolution was found for significantly wider aperture sizes. Area dose values varied significantly depending on the milling depth, the structure width, etc. and required careful calibration as IBL is in general less stable compared to EBL. Typically, 6 nm step sizes and an area dose of approximately 0.02 pC cm⁻² were used. All optical spectra shown throughout the manuscript were measured with a Fourier transform infrared spectrometer (Bruker Vertex 80), equipped with a microscope (Hyperion 3000) and a mercury cadmium telluride detector. Transmittance and reflectance were measured as unitless absolute quantities. The near-field simulations were performed using the frequency domain solver of CST Microwave Studio Suite 2018 in the wavelength range between 1 and 3.7 μ m. A unit cell was simulated with periodic boundary conditions in x- and y-directions for an infinite array and open boundary conditions in z to emulate free space. The experimental permittivity data for gold was taken from literature.^[57] As the experimental structure was embedded in glass, a background material was used in the simulation with $\epsilon = 2.25$ and $\mu = 1$.

Acknowledgements

The authors gratefully acknowledge financial support by the ERC Advanced Grant COMPLEXPLAS, Deutsche Forschungsgemeinschaft, Baden-Württemberg Stiftung, Ministerium für Wissenschaft, Forschung und Kunst Baden-Württemberg (ZAQuant, IQST), and Bundesministerium für Bildung und Forschung.

Open access funding enabled and organized by Projekt DEAL.

Conflict of Interest

The authors declare no conflict of interest.

Keywords

electron-beam lithography, fabrication schemes, ion-beam lithography, metasurfaces, nanofabrication, plasmonic nanostructures

Received: May 29, 2020

Revised: June 22, 2020

Published online: July 10, 2020

- [1] N. J. Halas, S. Lal, W.-S. Chang, S. Link, P. Nordlander, *Chem. Rev.* **2011**, *111*, 3913.
- [2] M. Kauranen, A. V. Zayats, *Nat. Photonics* **2012**, *6*, 737.
- [3] V. Giannini, A. I. Fernández-Domínguez, S. C. Heck, S. A. Maier, *Chem. Rev.* **2011**, *111*, 3888.
- [4] K. M. Mayer, J. H. Hafner, *Chem. Rev.* **2011**, *111*, 3828.
- [5] M. R. Jones, K. D. Osberg, R. J. Macfarlane, M. R. Langille, C. A. Mirkin, *Chem. Rev.* **2011**, *111*, 3736.
- [6] M. Rycenga, C. M. Cobley, J. Zeng, W. Li, C. H. Moran, Q. Zhang, D. Qin, Y. Xia, S. Yue, *Chem. Rev.* **2011**, *111*, 3669.
- [7] M. B. Cortie, A. M. McDonagh, *Chem. Rev.* **2011**, *111*, 3713.
- [8] A. Kuzyk, R. Schreiber, H. Zhang, A. O. Govorov, T. Liedl, N. Liu, *Nat. Mater.* **2014**, *13*, 862.
- [9] N. Liu, T. Liedl, *Chem. Rev.* **2018**, *118*, 3032.
- [10] D. B. Litt, M. Jones, M. Hentschel, Y. Wang, S. Yang, H. D. Ha, X. Zhang, A. P. Alivisatos, *Nano Lett.* **2018**, *18*, 859.
- [11] N. Li, A. Tittel, S. Yue, H. Giessen, C. Song, B. Ding, N. Liu, *Light: Sci. Appl.* **2014**, *3*, e226.
- [12] N. Liu, L. Langguth, T. Weiss, J. Kästel, M. Fleischhauer, T. Pfau, H. Giessen, *Nat. Mater.* **2009**, *8*, 758.
- [13] F. Falcone, T. Lopetegí, M. Laso, J. Baena, J. Bonache, M. Beruete, R. Marqués, F. Martín, M. Sorolla, *Phys. Rev. Lett.* **2004**, *93*, 197401.
- [14] K. Kumar, H. Duan, R. S. Hegde, S. C. W. Koh, J. N. Wei, J. K. W. Yang, *Nat. Nanotechnol.* **2012**, *7*, 557.
- [15] H. Duan, A. I. Fernández-Domínguez, M. Bosman, S. A. Maier, J. K. W. Yang, *Nano Lett.* **2012**, *12*, 1683.
- [16] J.-S. Huang, V. Callegari, P. Geisler, C. Brüning, J. Kern, J. C. Prangma, X. Wu, T. Feichtner, J. Ziegler, P. Weinmann, M. Kamp, A. Forchel, P. Biagioni, U. Sennhauser, B. Hecht, *Nat. Commun.* **2010**, *1*, 150.
- [17] N. Liu, T. Weiss, M. Mesch, L. Langguth, U. Eigenthaler, M. Hirscher, C. Sönnichsen, H. Giessen, *Nano Lett.* **2010**, *10*, 1103.
- [18] M. Horák, K. Bukvišová, V. Švarc, J. Jaskowiec, V. Křápek, T. Šikola, *Sci. Rep.* **2018**, *8*, 9640.
- [19] J. F. Einsle, J.-S. Bouillard, W. Dickson, A. V. Zayats, *Nanoscale Res. Lett.* **2011**, *6*, 572.
- [20] Y. Chen, K. Bi, Q. Wang, M. Zheng, Q. Liu, Y. Han, J. Yang, S. Chang, G. Zhang, H. Duan, *ACS Nano* **2016**, *10*, 11228.
- [21] E. J. R. Vesseur, R. de Waele, H. J. Lezec, H. A. Atwater, F. J. García de Abajo, A. Polman, *Appl. Phys. Lett.* **2008**, *92*, 083110.
- [22] B. Frank, P. Kahl, D. Podbiel, G. Spektor, M. Orenstein, L. Fu, T. Weiss, M. Horn-von Hoegen, T. J. Davis, F.-J. Meyer zu Heringdorf, H. Giessen, *Sci. Adv.* **2017**, *3*, e1700721.
- [23] T. J. Davis, D. Janoschka, P. Dreher, B. Frank, F.-J. Meyer zu Heringdorf, H. Giessen, *Science* **2020**, *368*, eaba6415.
- [24] S. Ristok, M. Roeder, S. Thiele, M. Hentschel, T. Guenther, A. Zimmermann, A. M. Herkommer, H. Giessen, *Opt. Lett.* **2020**, *45*, 1184.
- [25] N. Talebi, S. Meuret, S. Guo, M. Hentschel, A. Polman, H. Giessen, P. A. Van Aken, *Nat. Commun.* **2019**, *10*, 599.
- [26] N. Papisimakis, V. Fedotov, N. Zheludev, S. Prosvirnin, *Phys. Rev. Lett.* **2008**, *101*, 253903.
- [27] N. Verellen, Y. Sonnefraud, H. Sobhani, F. Hao, V. V. Moshchalkov, P. Van Dorpe, P. Nordlander, S. A. Maier, *Nano Lett.* **2009**, *9*, 1663.
- [28] S. Zhang, D. A. Genov, Y. Wang, M. Liu, X. Zhang, *Phys. Rev. Lett.* **2008**, *101*, 047401.
- [29] A. Litvak, M. Tokman, *Phys. Rev. Lett.* **2002**, *88*, 095003.
- [30] T. Zentgraf, T. Meyrath, a. Seidel, S. Kaiser, H. Giessen, C. Rockstuhl, F. Lederer, *Phys. Rev. B* **2007**, *76*, 033407.
- [31] N. A. Mirin, K. Bao, P. Nordlander, *J. Phys. Chem. A* **2009**, *113*, 4028.
- [32] B. Ögüt, N. Talebi, R. Vogelgesang, W. Sigle, P. A. van Aken, *Nano Lett.* **2012**, *12*, 5239.

- [33] M. Rahmani, D. Y. Lei, V. Giannini, B. Lukiyanchuk, M. Ranjbar, T. Y. F. Liew, M. Hong, S. A. Maier, *Nano Lett.* **2012**, *12*, 2101.
- [34] B. Luk'yanchuk, N. I. Zheludev, S. A. Maier, N. J. Halas, P. Nordlander, H. Giessen, C. T. Chong, *Nat. Mater.* **2010**, *9*, 707.
- [35] G. Cao, S. Dong, L. Zhou, Q. Zhang, Y. Deng, C. Wang, H. Zhang, Y. Chen, C. Qiu, X. Liu, *Adv. Opt. Mater.* **2020**, *8*, 1902153.
- [36] A. Lovera, B. Gallinet, P. Nordlander, O. J. F. Martin, *ACS Nano* **2013**, *7*, 4527.
- [37] B. Gallinet, O. J. F. Martin, *Phys. Rev. B* **2011**, *83*, 235427.
- [38] J. A. Fan, C. Wu, K. Bao, J. Bao, R. Bardhan, N. J. Halas, V. N. Manoharan, P. Nordlander, G. Shvets, F. Capasso, *Science* **2010**, *328*, 1135.
- [39] M. Hentschel, M. Saliba, R. Vogelgesang, H. Giessen, A. P. Alivisatos, N. Liu, *Nano Lett.* **2010**, *10*, 2721.
- [40] J. B. Lassiter, H. Sobhani, J. A. Fan, J. Kundu, F. Capasso, P. Nordlander, N. J. Halas, *Nano Lett.* **2010**, *10*, 3184.
- [41] K. Thyagarajan, J. Butet, O. J. F. Martin, *Nano Lett.* **2013**, *13*, 1847.
- [42] H. Liu, E. S. P. Leong, Z. Wang, G. Si, L. Zheng, Y. J. Liu, C. Soci, *Adv. Opt. Mater.* **2013**, *1*, 978.
- [43] M. Hentschel, T. Weiss, S. Bagheri, H. Giessen, *Nano Lett.* **2013**, *13*, 4428.
- [44] F. Wen, Y. Zhang, S. Gottheim, N. S. King, Y. Zhang, P. Nordlander, N. J. Halas, *ACS Nano* **2015**, *9*, 6428.
- [45] A. Kuzyk, R. Schreiber, Z. Fan, G. Pardatscher, E.-M. Roller, A. Högele, F. C. Simmel, A. O. Govorov, T. Liedl, *Nature* **2012**, *483*, 311.
- [46] Y. Y. Lee, R. M. Kim, S. W. Im, M. Balamurugan, K. T. Nam, *Nanoscale* **2020**, *12*, 58.
- [47] M. Hentschel, M. Schäferling, X. Duan, H. Giessen, N. Liu, *Sci. Adv.* **2017**, *3*, e1602735.
- [48] V. K. Valev, J. J. Baumberg, C. Sibilia, T. Verbiest, *Adv. Mater.* **2013**, *25*, 2517.
- [49] L. V. Besteiro, H. Zhang, J. Plain, G. Markovich, Z. Wang, A. O. Govorov, *Adv. Opt. Mater.* **2017**, *5*, 1700069.
- [50] Z. Xu, L. Xu, L. M. Liz-Marzán, W. Ma, N. A. Kotov, L. Wang, H. Kuang, C. Xu, *Adv. Opt. Mater.* **2013**, *1*, 603.
- [51] V. A. Fedotov, A. S. Schwanecke, N. I. Zheludev, V. V. Khardikov, S. L. Prosvirnin, *Nano Lett.* **2007**, *7*, 1996.
- [52] S. Zhang, J. Zhou, Y.-S. Park, J. Rho, R. Singh, S. Nam, A. K. Azad, H.-T. Chen, X. Yin, A. J. Taylor, X. Zhang, *Nat. Commun.* **2012**, *3*, 942.
- [53] Y. Luo, C. Chi, M. Jiang, R. Li, S. Zu, Y. Li, Z. Fang, *Adv. Opt. Mater.* **2017**, *5*, 1700040.
- [54] J. K. Gansel, M. Thiel, M. S. Rill, M. Decker, K. Bade, V. Saile, G. von Freymann, S. Linden, M. Wegener, *Science* **2009**, *325*, 1513.
- [55] M. Decker, M. Ruther, C. E. Kriegler, J. Zhou, C. M. Soukoulis, S. Linden, M. Wegener, *Opt. Lett.* **2009**, *34*, 2501.
- [56] J. Karst, N. Strohfeldt, M. Schäferling, H. Giessen, M. Hentschel, *Adv. Opt. Mater.* **2018**, *6*, 1800087.
- [57] P. B. Johnson, R. W. Christy, *Phys. Rev. B* **1972**, *6*, 4370.